Materials Today Bio 16 (2022) 100396

Contents lists available at ScienceDirect

Materials Today Bio

journal homepage: www.journals.elsevier.com/materials-today-bio

Redox homeostasis modulation using theranostic AIE nanoparticles results in positive-feedback drug accumulation and enhanced drug penetration to combat drug-resistant cancer

Shaoqing Chen [a,b,1], Ziyu Wang [d,1], Li Liu [e], Yuting Li [e], Xinye Ni [a,b,**], Hong Yuan [c,***], Cheng Wang [e,*]

[a] Second People's Hospital of Changzhou, Nanjing Medical University, Changzhou, Jiangsu, China
[b] Jiangsu Province Engineering Research Center of Medical Physics, Changzhou, Jiangsu 213003, China
[c] College of Pharmaceutical Sciences, Zhejiang University, Yuhangtang Road 866, Hangzhou, Zhejiang, China
[d] State Key Laboratory of Radiation Medicine and Protection, School for Radiological and Interdisciplinary Sciences (RAD-X), Soochow University, 199 Ren'ai Road, Suzhou, Jiangsu, China
[e] School of Pharmacy, Changzhou University, Changzhou, Jiangsu, China

ARTICLE INFO

Keywords:
Redox homeostasis modulation
Multidrug drug resistance
Drug delivery systems
Positive-feedback
Aggregation-induced emission

ABSTRACT

Drug-resistant cancers usually have multiple barriers to compromise the effect of therapies, of which multidrug-resistance (MDR) phenotype as the intracellular barrier and dense tumor matrix as the extracellular barrier, significantly contribute to the poor anticancer performance of current drug delivery systems (DDS). Here in this study, we fabricated a novel aggregation-induced emission (AIE)-active polymer capable of self-assembling into ultrasmall nanoparticles (~20 nm) with D-alpha Tocopheryl Polyethylene Glycol Succinate (TPGS), for dual-encapsulating of doxorubicin (Dox) and sulforaphane (SFN) (AT/Dox/SFN). It revealed that redox homeostasis modulation of MDR cells (MCF-7/Adr) using AT/Dox/SFN can trigger mitochondria damage and ATP deficiency, which reverse the MDR phenotype of MCF-7/Adr cells to afford enhanced cellular uptake of both drug and DDS in a positive-feedback manner. The enhanced cellular drug accumulation further initiates the "neighboring effect" for improved drug penetration. Using this strategy, the growth of *in vivo* MCF-7/Adr tumors can be effectively inhibited at a low dosage (1/5) of doxorubicin (Dox) as compared to free Dox. In summary, we offer a new approach to overcome both the intracellular and extracellular barriers of drug-resistant cancers and elucidate the potential action mechanisms, which are beneficial for better cancer management.

1. Introduction

Recent studies in experimental and clinical cancer therapies have revealed that multidrug-resistance (MDR) is a typical phenotype occurred in many cancer types, which is the primary reason responsible for the failure of many current cancer chemotherapies [1,2]. It was reported that the highly elevated concentration of reducing substances, such as glutathione (GSH) [3], maintain delicate redox homeostasis within the MDR cancer cells [4]. It was also well recognized that redox homeostasis exerts substantial diversity of roles in fundamental cellular physiology, contributes to the development of malignant phenotypes, and is positively related to the proliferation, metastasis, and invasion processes of MDR cells [5,6], for example higher reactive oxygen species (ROS) was found to shape the tumor microenvironment and affect the growth of BRCA1-associated breast cancer [6]. The detoxification effect of high concentration of intracellular GSH on chemotherapy drugs is gaining more and more attention. Many previous studies have proven that reducing intracellular GSH concentration can exert beneficial effects on restoring the chemosensitivity of cancer cells [7,8]. Moreover, considering the deep involvement of GSH in maintaining the normal function of cancer cells, the modulation of redox homeostasis might not only restore the chemosensitivity of cancer cells but also hold the

* Corresponding author.
** Corresponding author. Second People's Hospital of Changzhou, Nanjing Medical University, Changzhou, Jiangsu, China.
*** Corresponding author.
E-mail addresses: nxy@njmu.edu.cn (X. Ni), yuanhong70@zju.edu.cn (H. Yuan), wangc90@cczu.edu.cn (C. Wang).
[1] These authors contributed equally to this work.

https://doi.org/10.1016/j.mtbio.2022.100396
Received 7 June 2022; Received in revised form 7 August 2022; Accepted 8 August 2022
Available online 14 August 2022

potential to regulate the cancer phenotype through other mechanisms and beneficial for cancer treatment [9–11].

Sulforaphane (SFN) is a naturally occurring isothiocyanate enriched in broccoli [12]. It is well-recognized to be a mild cancer prevention drug, which reverses the progression of cancer cells through mechanisms including activation of antioxidant enzymes and induction of cell cycle arrest/cell apoptosis [13,14]. Most importantly, it was reported that SFN could effectively form GSH-SFN complex with GSH [15], which was able to realize GSH depletion. In addition, D-alpha Tocopheryl Polyethylene Glycol Succinate (TPGS), as a widely applied derivative of vitamin E, is well-known to selectively induce ROS stress on cancer cells instead of normal ones [16,17]. In addition, TPGS as an amphiphilic molecule was applied to form mixed nanoparticles (such as mixed micelle) with other materials to offer further optimizations in functional properties to improve the performance of the mixed nanoparticles [18]. Based on these studies, it was suggested that the introduction of both SFN and TPGS in the drug delivery systems (DDS) was able to effectively modulate the redox homeostasis and reverse the MDR of target cells.

Despite the MDR as an intracellular barrier, the tumor tissue as a whole also develops versatile protection barriers to impair the functionality of extraneous DDSs [19,20], of which dense tumor matrix, as the most widely studied one, usually impedes the penetration of nanoparticles to give off-threshold drug concentration in deep tumor tissues [21]. It has been reported by previous studies that nanoparticles with sizes smaller than 50 nm showed better tumor penetration capacity [11,22]. However, considering the clearance limit of the kidney at around 5 nm, the construction of DDS falls at the lower limits of the size range between 5 and 50 nm, is highly desirable but challenging [23]. Moreover, devising DDS with strong "neighboring effect" was also considered as another effective way to increase the penetration of drugs [24,25]. The combination of both strategies using one DDS might offer enhanced tumor penetration performance upon *in vivo* practice.

Based on the recently quick development of aggregation-induced emission (AIE) polymers and their suitability to construct DDSs [26], here in our study, a new AIE polymer was first synthesized as a bone material (Fig. 1A). Together with TPGS, the AIE polymer can self-assemble into ultrasmall nanoparticles with size of around 20 nm (AT). At the same time, the hydrophobic core of AT also afforded the encapsulation of both SFN and doxorubicin (Dox) to construct a DDS for multifunctional cancer therapy (AT/Dox/SFN). It was suggested that the AIE nature of the polymer could self-indicate its location upon administration, while the drug release of Dox could be reflected by the changes of fluorescence resonance energy transfer (FRET) between AIE and Dox. Upon accumulation at the tumor tissue through enhanced penetration and retention (EPR) effect, the internalized SFN and TPGS could modulate the intracellular redox homeostasis of cells to elevate the ROS level, which finally induced mitochondria damage and the following ATP deficiency. The drop in ATP supply further decreased the excretion of drugs as well as the expression of MDR-related proteins (such as P-gp) to allow enhanced cellular uptake of more drugs and DDS in a positive-feedback way. The enhanced intracellular drug accumulation further initiates "neighboring effect" in tumor tissues for improved drug penetration. Cooperated with its size advantage, the AT/Dox/SFN was shown to overcome the extracellular barrier of the dense tumor matrix to realize drug delivery into the deep tumor tissue (Fig. 1B). Owning to the above advantages, the AT/Dox/SFN could effectively suppress the proliferation of MCF-7/Adr cells *in vitro* in a synergetic manner, and especially, was demonstrated to significantly inhibit the growth of *in vivo* MCF-7/Adr tumor effectively under low Dox dosage.

2. Results and discussion

2.1. Synthesis of AIE polymer and characterization of nanoparticles

The detailed synthetic route of AIE-active polymer was outlined in Fig. 1A. The monomers **M-1**, **M-2**, and **M-3** were synthesized *via* the methods in previous literature [27]. The conjugated polymer was synthesized using **M-1**, **M-2** and **M-3** *via* Suzuki coupling reaction to give the product (0.244 g). In the ^{1}H NMR spectrum of the polymer (Figure S1), a single high peak appeared at 3.66 ppm, which could be assigned to the PEG chains. This result can confirm the successful combination of PEG chains. According to the conjugated polymer, different moieties have their functions: i) the conjugated backbone decides the optical property of the conjugated polymer, and ii) the PEG moiety as the hydrophilic group [28]. The molecular weight of the polymer was determined using GPC (Figure S2). The results demonstrated that the M_w = 6800, M_n = 4610, and polydispersity index (PDI) of 1.47.

Afterward, the UV–vis absorption spectrum and the fluorescence emission spectra of the AIE polymer were outlined in Fig. 2. As was shown in Fig. 2A, an absorption peak appeared at 377 nm, which could be assigned to the conjugated backbone [29]. According to the fluorescence emission spectra, the conjugated polymer exhibited apparent AIE behavior and gave the emission peak around 502 nm, which gradually enhanced as the water fraction (f_w) increased from 0% to 99% (Fig. 2B).

Afterward, the TPGS was mixed with the AIE polymer to prepare nanoparticles (AT) where the drugs (Dox and SFN) were loaded into AT during the self-assembly process as the hydrophobic nature of AIE molecules and vitamin E offered a suitable harbor for the loading of hydrophobic drugs. As shown in Fig. 2C, the obtained AT/Dox/SFN showed narrow size distribution at around 20 nm with a PDI of 0.037. The morphology observation using TEM (Fig. 2D) and SEM (Figure S3) also demonstrated a similar conclusion. It also revealed that the nanoparticles were in spheroid shape with clear boundaries with one another [30]. The zeta potential of AT/Dox/SFN was close to neutral (−1.13 mV), which

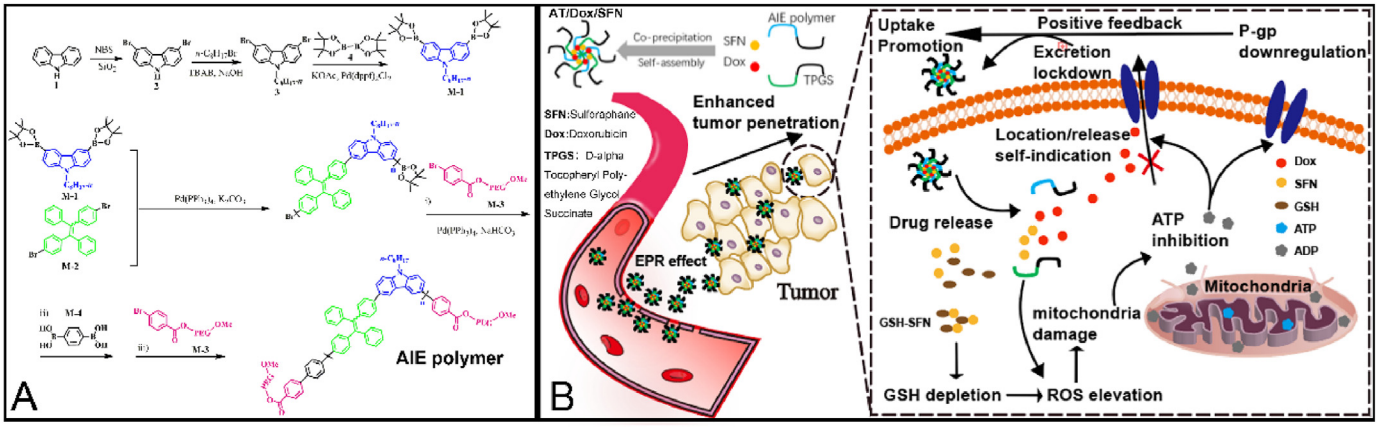

Fig. 1. (A) The detailed synthetic route of AIE polymer. (B) The schematic illustration of the assembly and action mechanism of AT/Dox/SFN.

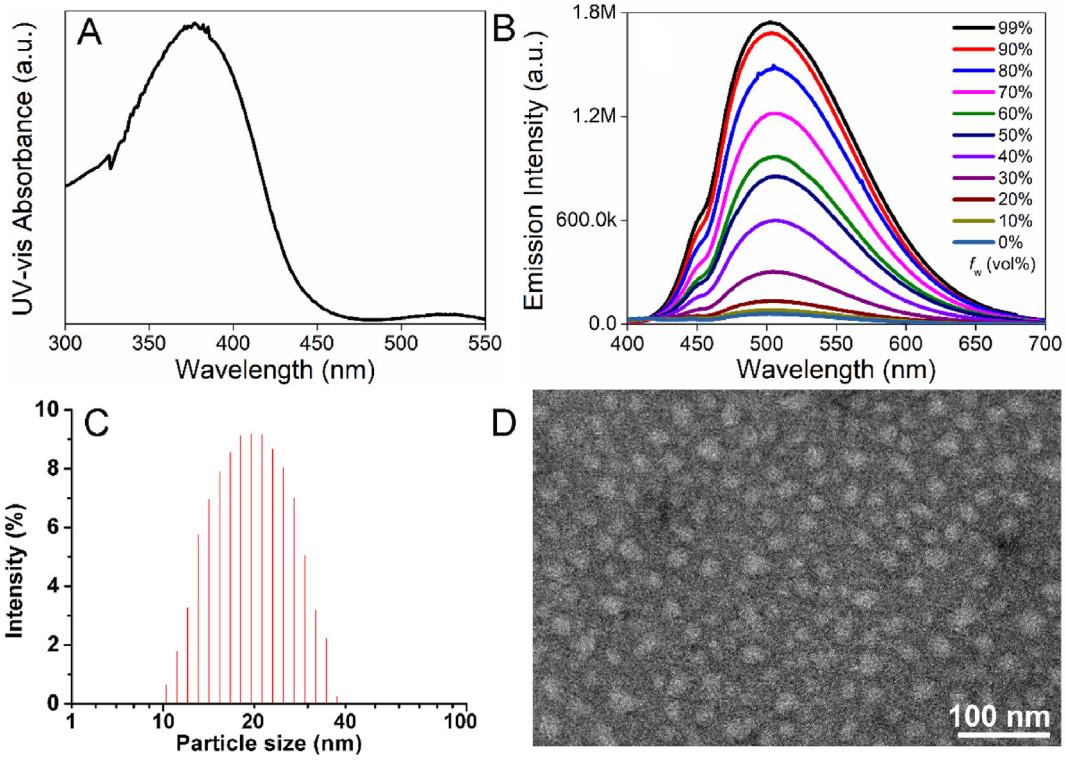

Fig. 2. Characterization of polymer and nanoparticles. The UV–vis absorption spectra (A) and fluorescence emission spectra (B) of the AIE polymer. The particle size distribution (C) and TEM image (D) of AT/Dox/SFN. Scale bar: 100 nm.

might ascribe to the surface modification of the PEG chain. According to previous reports, the neutral and hydrophilic nature of PEG can significantly increase the stability of the modified system to provide shielding and protection to avoid premature excretion [31], [32]. As a result, the AT/Dox/SFN with PEG modification was expected to take full advantage of the EPR effect of tumor tissue for targeted tumor accumulation. The particle size, zeta potential as well as PDI of other similar nanoparticles were summarized in Table S1. It was observed that the loading of both drugs did not significantly change the size and surface properties of the nanoparticle, which indicated that single-loaded nanoparticles (AT/Dox and AT/SFN) with similar size and zeta potential were promising controls to AT/Dox/SFN. However, it was also noticed that the size of AIE/-Dox/SFN was twice that of AT/Dox/SFN, indicating that the introduction of TPGS might offer contributions to the optimization of nanoparticle size, which was in line with previous studies [33,34].

To further reveal the characteristics of the AT/Dox/SFN, its long-term colloidal stability and hemolysis against RBCs were also investigated. To estimate the colloidal stability, the size changes of AT/Dox/SFN, which reflected the integrity of DDS, were monitored under physiological conditions (PBS at pH 7.4 and 10% mouse plasma) for 7 days. As shown in Figure S4, AT/Dox/SFN showed high stability in both PBS and plasma, as supported by the minor fluctuations in particle size. These results demonstrated that AT/Dox/SFN is a highly stable system under physiological environments and might be suitable as DDS for cancer therapy. Moreover, a hemolysis assay was also conducted to test the biocompatibility of AT/Dox/SFN. As shown in Figure S5, only neglectable hemolysis (<3%) was observed even at the highest AT/Dox/SFN concentration of 1 mg/mL, which suggested the preferable biocompatibility of this platform for *in vivo* applications.

2.2. Self-indication of location and drug release

According to previous literature, Dox shows an apparent absorption wave in the region of 400–600 nm and gives an absorption peak centered around 485 nm, which can well overlap with the fluorescence spectrum of AIE polymer [35]. Therefore, a FRET process can be built from AIE polymer to Dox, which can be applied in monitoring the drug delivery process. The fluorescence spectra of AT/Dox with different Dox ratios (charge ratio) were carried out in Fig. 3A. The fluorescence emission could be gradually quenched as the Dox ratio increased, indicating the successful building of the FRET process from the AIE polymer to Dox. Besides, a new emission peak centered at 550 nm could be observed, which can be assigned to Dox. These results suggested that the FRET process could be applied in drug-releasing monitoring. As a proof of concept, the fluorescence profile of free Dox, drug-free carrier (AT) and AT/Dox/SFN were investigated. As shown in Fig. 3B, free Dox only showed fluorescence in the acceptor channel (Ex = 559 nm/Em = 575–675 nm) while the fluorescence signal of AT was only observed in the donor channel (Ex = 405 nm/Em = 422–522 nm). By contrast, it was noted that the fluorescence signal in the donor channel was slightly quenched in AT/Dox/SFN as compared to AT. In addition, fluorescence signals could be obtained from both the FRET channel (Ex = 405 nm/Em = 575–675 nm) and the acceptor channel, which suggested that Dox was not only successfully being loaded into the DDS, but also formed intermolecular FRET with AT. To further study whether the changes in the FRET signal can be employed as a signal to reveal the drug release of AT/Dox/SFN, the time-dependent intracellular signals (donor and FRET) were monitored. As shown in Fig. 3C, the intracellular accumulation of AT/Dox/SFN was positively related to incubation time. However, the FRET signal at different time intervals varied since it was affected by both intracellular AT concentration and drug release degree. To normalize the influence of AT and reveal the dynamic intracellular drug release profile, the ratio of mean fluorescent intensity in the FRET channel (F_{Red}) and mean fluorescent intensity in the donor channel (F_{Blue}) were calculated and plotted against time. As displayed in Fig. 3D, the F_{Red}/F_{Blue} value gradually decreased as a function of time, which suggested that the FRET signal decreased as time extended. It was reported that the departure of Dox from the DDS would weaken the intracellular FRET effect (between

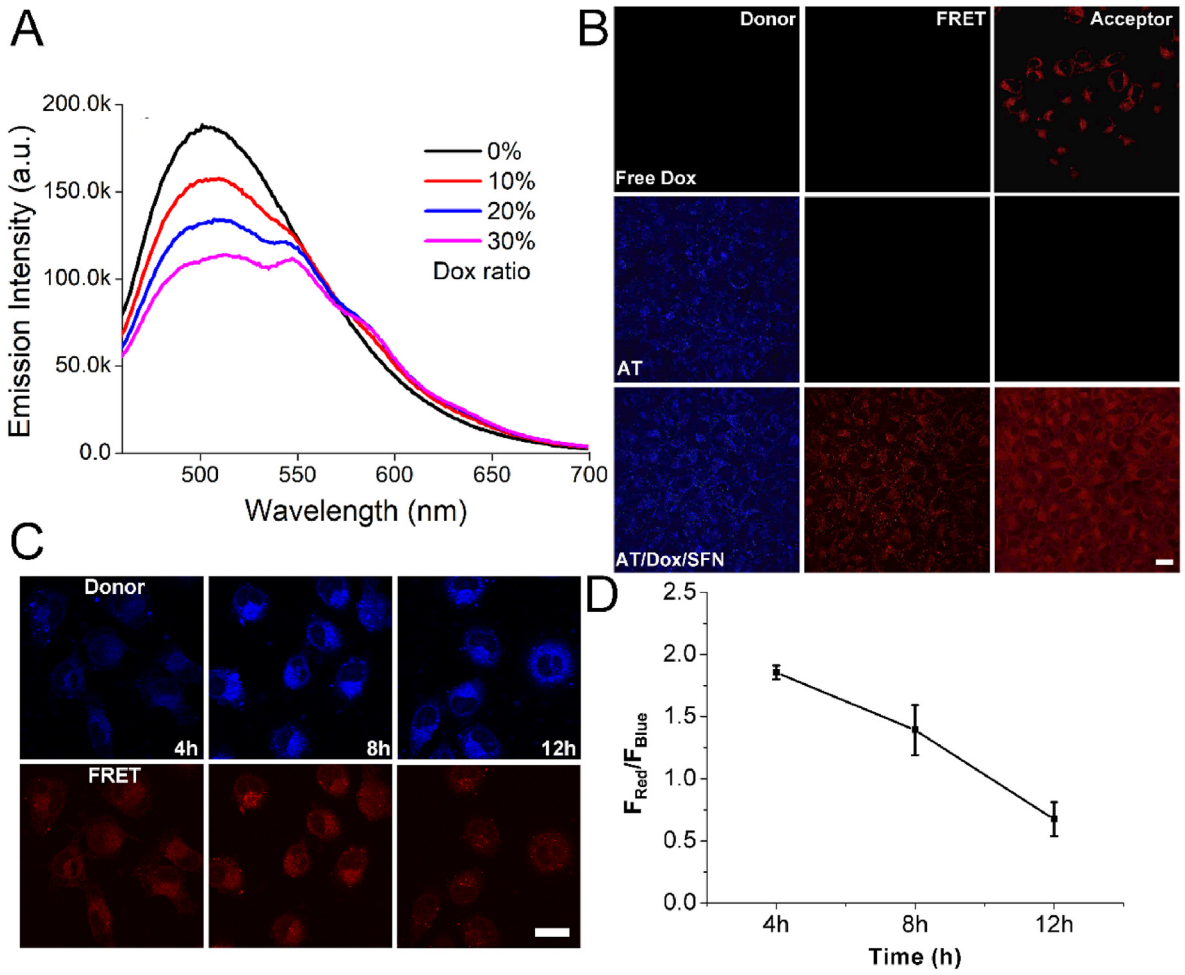

Fig. 3. AT/Dox/SFN self-indicated its location and drug release. (A) The relationship between the fluorescence emission spectra of AT/Dox/SFN and the charged ratios of Dox. (B) Fluorescent images of MCF-7/Adr cells incubated with free Dox (upper), AT (middle) or AT/Dox/SFN (lower) for 8 h. For each panel, left: AIE (donor); middle: FRET; right: Dox (acceptor). (C) Fluorescent images of time-dependent *in vitro* cellular uptake of AT/Dox/SFN in MCF-7/Adr cells. Blue channel: FTP; red channel: FRET. Scale bar: 20 μm. (D)The ratio of mean fluorescent intensity in FRET channel (F_{Red}) and mean fluorescent intensity in donor channel (F_{Blue}) as a function of time indicated the intracellular drug release.

AT and Dox) and therefore give a reduced signal [36]. As a result, the decrease of F_{Red}/F_{Blue} value suggested the increased drug release as a function of time, which was in line with previous reports [37,38] and our *in vitro* release studies (Figure S6). Based on these results, it was concluded that AT/Dox/SFN was capable of self-reporting its intracellular drug release profile in a real-time manner.

2.3. AT/Dox/SFN modulated the redox intracellular redox homeostasis of MCF-7/Adr cells

To confirm the redox modulation effects using TPGS and SFN, the free SFN, TPGS as well as AT/SFN were selected to independently study the benefits of mono or combined application of these materials. The intracellular ROS level after treatment with different samples for various time intervals was firstly investigated. As shown in Fig. 4A, consistent with the previous report and our conjecture [15,16], both SFN and TPGS could increase the ROS level within cells in a time-dependent manner. Moreover, the combination of both materials using DDS further potentiated this effect as AT/SFN showed a much higher elevated intracellular ROS level than either SFN or TPGS alone at both time intervals. This observation was also confirmed by quantitative analysis of intracellular GSH concentration at 12 h post-treatment. As shown in Fig. 4B, intracellular GSH concentration in AT/SFN treated MCF-7/Adr cells dropped to a much lower level than in other groups, suggesting that the proposed redox modulation was successfully realized using our DDS. However, as redox hemostasis is intensively involved in the normal functions of cellular physiology, it was suggested that the redox modulation might have a further significant impact on the phenotype of cells [39]. Considering ATP as a universal energy currency in all cells and was widely reported to have a deep relation with MDR [40,41], the change in ATP level might reverse the MDR of cells and have a further profound influence on cell survival. As a result, the mitochondria as the generator of ATP were selected as the target. The mitochondria damage characterized as swelling can be identified as a decrease in OD_{530nm} compared to control. As demonstrated in Fig. 4C, both SFN and TPGS showed specific damage to mitochondria with a time-dependent decrease of OD_{530}. Most importantly, the combination of SFN and TPGS in AT/SFN contributed to the most significant swelling of mitochondria in MCF-7/Adr cells. This conclusion was also verified by the staining of mitochondria damage using JC-1 (Figure S7). Subsequently, the changes in ATP content resulting from mitochondria malfunction were also assessed. As demonstrated in Fig. 4D, similar to that of mitochondria swelling assay, the ATP content in both SFN and TPGS groups decreased as a function of time. In particular, the AT/SFN group with the most significant mitochondria malfunction also showed the lowest ATP content, which was merely 52.35% at 12 h post incubation, indicating the significant mitochondria malfunction of AT/SFN could interrupt the energy supply of cells.

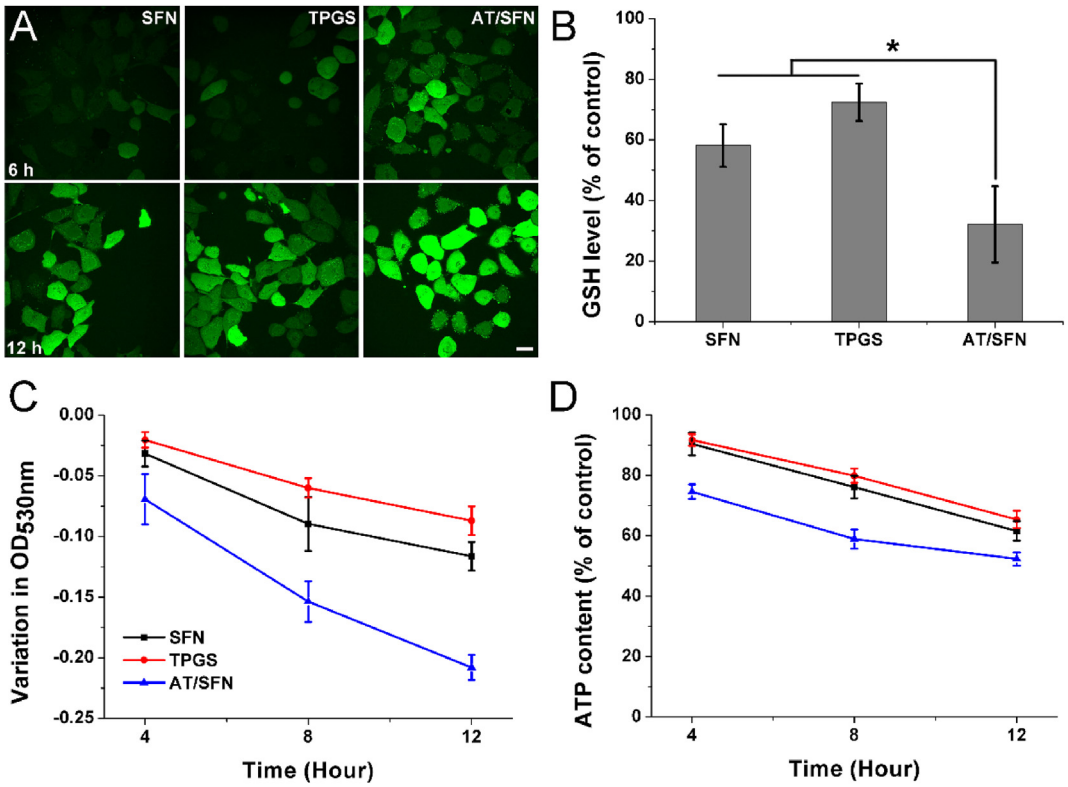

Fig. 4. AT/Dox/SFN modulated the redox intracellular redox homeostasis of MCF-7/Adr cells to induce mitochondria damage and ATP deficiency. (A) The time-dependent intracellular ROS level after treatment with SFN, TPGS and AT/SFN. Scale bars: 20 μm. (B) The intracellular GSH level (% of control) after treated with SFN, TPGS and AT/SFN for 12 h $*P < 0.05$. Swelling test of mitochondria damage (C) and determination of intracellular ATP content (D) after MCF-7/Adr cells treated with SFN, TPGS and AT/SFN for different time intervals (4, 8 and 12 h).

2.4. MDR reversion and positive-feedback manner for enhanced drug/nanoparticle uptake

To study the impact of redox modulation on the reverse of MDR, MCF-7/Adr cells were firstly treated with the above-mentioned materials for 12 h and then incubated with free Dox for another 4 h. The Dox accumulation within cells was visualized using CLSM (Fig. 5A). Compared with the control group, the elevated Dox accumulation in different experimental groups indicated different degrees of MDR reversion. In line with the results in Fig. 4, the AT/SFN could effectively reverse the MDR phenotype of MCF-7/Adr cells to allow a preferable accumulation of free drugs within cells.

This result further inspired us to investigate the enhanced nanoparticle uptake of cells resulting from MDR reversion. If this was feasible, the further accumulated nanoparticles might persistently reinforce this process to afford further enhanced nanoparticle uptake in a positive-feedback manner. As a proof of concept, the MCF-7/Adr tumor-bearing nude mice were intratumorally administrated with AT/SFN for different time intervals. The tumor tissues were then collected and treated with Collagenase. The obtained cells were then incubated with AT/Dox/SFN for another 4 h, and the intracellular accumulation of Dox was observed. As shown in Fig. 5B, AT/SFN treatment for 12 h significantly increased the following cellular uptake of nanoparticles (AT/Dox/SFN) as compared to the control group, and this effect was further potentiated as time extended to 12 h, which suggested the positive-feedback manner of enhanced cellular uptake upon redox modulation. Consistently, the tumor tissue-derived cells also showed enhanced cellular accumulation of AT/Dox/SFN after being pretreated with AT/SFN in a time-dependent manner.

To illuminate the possible mechanisms of redox modulation in reversing the MDR cells, the expression of P-gp in obtained cells and tissues was evaluated. As shown in Fig. 5D and E and Figure S8, compared to the control group, the incubation with AT/SFN could significantly reduce the expression of P-gp in cells in a time dependent manner. It was well-recognized that P-gp is an important efflux pump, which contributes significantly to the MDR of cells [42]. Therefore, the reduced expression of P-gp as a result of redox modulation was suggested to be responsible for the reduction of resistant capacity in MCF-7/Adr cells.

2.5. Neighboring effect and size advantage enhanced drug penetration of AT/Dox in tumor tissue

According to our previous report and other parallel studies, the "neighboring effect", characterized as a small portion of cells that take up nanoparticles becoming in situ drug depots to further release active drugs/nanoparticles to surrounding cells, maybe a common phenomenon in DDS-mediated cancer therapy [25]. As a result, the reverse of MDR for enhanced drug accumulation within cells might be hopeful to augment this effect that contributes to positive benefits in cancer therapy. Moreover, the positive-feedback manner of nanoparticle uptake resulting from redox modulation was also supposed to enhance the "neighboring effect" in cancer therapy. In support of our hypothesis, the intercellular apoptosis induced by AT/Dox/SFN was investigated using coverslips. In brief, MCF-7/Adr cells seeded on coverslip A were pre-incubated with free Dox or AT/Dox/SFN for different time intervals (12 and 24 h) and then co-incubated with the neighboring coverslip B with fresh cells for another 24 h, followed by observation using CLSM. As shown in Fig. 6A, in contrast to the free Dox group under the same condition, Annexin V-FITC staining revealed that AT/Dox/SFN could effectively induce apoptosis of neighboring cells (B). In addition, this effect was also positively related to incubation time, confirming the suggestion that the positive-feedback manner of AT/Dox/SFN uptake could contribute positive effects in augmenting the "neighboring effect" of this platform.

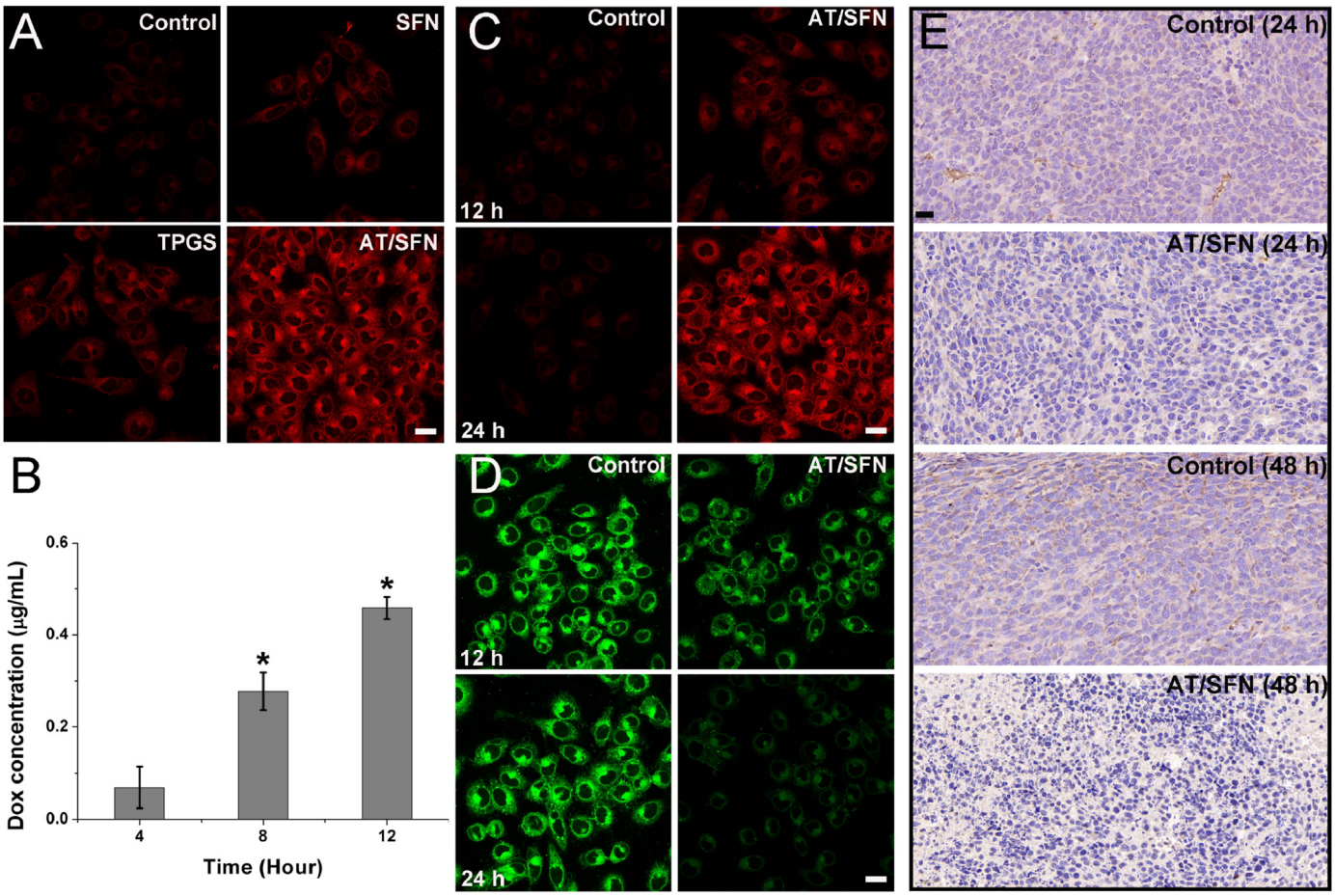

Fig. 5. Redox modulation reversed the MDR of MCF-7/Adr cells and induced positive-feedback uptake of drug/nanoparticle. (A) The intracellular accumulation of free Dox at 4 h post-incubation after cells were pre-treated with SFN, TPGS, and AT/SFN for 12 h. (B) The cellular uptake of AT/Dox/SFN (indicated by intracellular Dox concentration) after cells were pre-treated with AT/SFN for different time intervals (4, 8 and 12 h). *$P < 0.05$ versus 4 h. The cellular uptake of AT/Dox/SFN (C) and P-gp expression level (D) in cancer cells (derived from tumor tissue) after intratumoral injection with AT/SFN for different time intervals (12 and 24 h). (E) The P-gp expression level of tumor tissues after intratumoral injection with AT/SFN for different time intervals (24 and 48 h). Scale bars: 20 μm.

It was reported that nanoparticles that exert strong neighboring effects were able to enhance drug penetration in the tumor, like "peeling an onion" layer by layer [43]. Considering the enhanced "neighboring effect" and the size advantage of AT/Dox/SFN, the drug penetration of this platform might be significantly elevated. To verify our hypothesis, MCTSs mimicking the structure of the solid tumor, were employed as the model to study the penetration ability of AT/Dox/SFN. As shown in Fig. 6B, free DOX only showed moderate penetration in MCTSs with most of the drug distribution at the periphery and undetectable signals in the core region. This might be due to the strong MDR nature of MCF-7/Adr cells as well as the poor "neighboring effect" of free Dox. In contrast, AT/Dox/SFN showed a significantly enhanced penetration profile with apparent Dox fluorescence spread in most regions, even 90 μm from the surface towards the middle, indicating that the drug molecules could be readily delivered into deep tumor tissue.

In support of our hypothesis *in vivo*, after intratumoral injection of free Dox or AT/Dox/SFN to the tumor tissue, the neighboring tumor tissues were harvested, and the comparative penetration of the drug was studied. As shown in Fig. 6C, the Dox signal could be observed in both groups on the superficial layer. However, the Dox signal in the free Dox group significantly decreased when the depth extended to 500 μm, and merely no Dox signal can be observed in further increased depths. In contrast, Dox distribution could be observed in every tumor section of AT/Dox/SFN treated sample, even at 1000 μm below the superficial layer. To eliminate the influence of high angiogenesis of tumors, we also stained the blood vessels (CD31 staining) of the tumor sections and compared the distribution of Dox in both groups. As illustrated in Fig. 6D, AT/Dox/SFN showed superior ability on tumor penetration of Dox than free drug, as supported by the significant difference in drug distribution around blood vessels [25]. In detail, Dox delivered by AT/Dox/SFN was distributed evenly in the tumor tissues outside of the tumor vasculature, while the free drug was mainly accumulated in or near the tumor vasculature. Collectively, AT/Dox/SFN was capable of efficiently delivering the drug cargo from the exterior to the interior of the solid tumor, which was beneficial to elevate its anticancer efficacy.

2.6. *In vitro anticancer performance*

To investigate the anticancer effect of the AT/Dox/SFN, the cell viability of MCF-7/Adr cells treated with different formulations for 48 h at various drug concentrations was recorded using the MTT assay. The cell viability of the newly synthesized AIE was assessed prior to the anticancer assay. In line with previous studies [44,45], AIE polymers (Figure S9) showed negligible cytotoxicity (cell viability over 90%) even after being incubated with MCF-7/Adr cells for 48 h at a concentration of 200 μg/mL, which suggested the preferable biocompatibility of the AIE polymer. As shown in Fig. 7A, in the case of free Dox, due to the strong MDR nature of MCF-7/Adr cells, the cell viability of treated cells was over 90% even at the highest drug concentration of 5 μM. The Dox delivery using AT (AT/Dox) significantly enhanced the anticancer efficacy with a

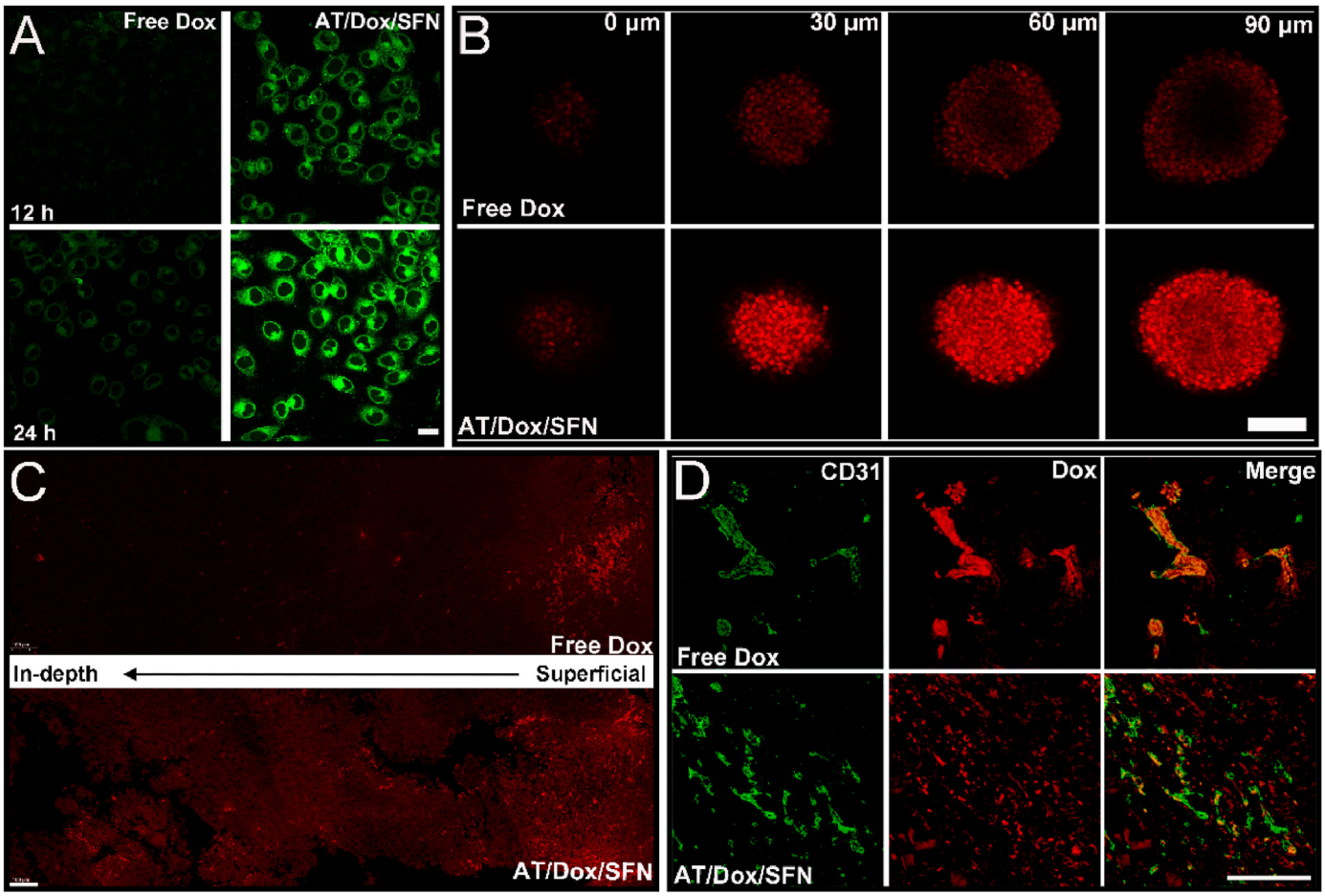

Fig. 6. Neighboring effect and size advantage enhanced drug penetration of AT/Dox/SFN in tumor tissue. (A) The positive-feedback manner enhanced the neighboring effect of AT/Dox/SFN. The neighboring apoptotic cells were stained by Annexin V-FITC (green channel). Scale bar: 20 μm. (B) *In vitro* penetration of Dox into the MCTSs after incubation with free Dox and AT/Dox/SFN. Scale bar: 200 μm. (C) *In vivo* penetration of Dox into the different tumor depths after intratumoral injection of free Dox and AT/Dox/SFN for 48 h. Scale bar: 50 μm. (D) *In vivo* distribution of Dox from the neighboring blood vessels following intratumoral injection of free Dox and AT/Dox/SFN for 48 h. The blood vessels were stained by the FITC-CD31 antibody. Scale bar: 50 μm.

moderate performance at the same drug concentration, suggesting the beneficial effect of DDS on the delivery of drugs. As expected, AT/Dox/SFN integrating the benefits of both SFN and TPGS exerted the most potent cytotoxic effect on MCF-7/Adr cells. The optical observations of cell morphology in Fig. 7B also reached similar conclusions.

The cytotoxicity of different treatments to the MCTSs model was further assessed to demonstrate the desirable *in vitro* cytotoxicity of AT/Dox/SFN. Unlike the other groups, especially free Dox, which all showed continuous growth in the MCTSs volume, the group treated with AT/Dox/SFN showed the best cytotoxicity effect with decreased MCTSs volume at the end of the test (Fig. 7C). Moreover, as shown in Fig. 7D, the expression of γ-H2AX (a marker of DNA damage), cytochrome (Cyto C) and cleaved PARP (C-PARP) were up-regulated after AT/SFN or AT/Dox treatment, suggesting the elevated level of cell apoptosis. However, AT/Dox/SFN treatment led to a more significant increased expression of these apoptosis-related proteins, demonstrating the supportive role of SFN to augment Dox-mediated cell apoptosis. This conclusion was also verified by the opposite trends of Bcl-2, a rescue protein against apoptosis. It was inferred that the combination of MDR reversion, enhanced "neighboring effect" as well as the size advantages in AT/Dox/SFN could not only effectively induce apoptosis to the superficial cells, but also preferably infiltrate into the next layer to repeat this process, which offered an efficient approach to penetrate deep tissue to achieve uniform distribution of drug at both extracellular and intracellular areas for enhanced anticancer outcomes [46].

2.7. *In vivo* tumor homing and anticancer assays

To estimate the *in vivo* performance of AT/Dox/SFN, the DiR as a fluorescent probe was loaded into AT/Dox/SFN to help monitor the real-time *in vivo* distribution of AT/Dox/SFN on the MCF-7/Adr oxgraft model. As displayed in Fig. 8A, AT/Dox/SFN showed promising tumor-homing capability at merely 6 h post-injection. Extended time intervals resulted in a more intense fluorescence signal in the tumor tissue. The semiquantitative analysis of organ distribution was performed using *ex vivo* imaging at 48 h post-injection. As shown in Fig. 8B, the AT/Dox/SFN was mainly accumulated in the tumor tissue without significant retention in the major organs, suggesting the promising tumor-homing property of this DDS. The *in vivo* anticancer assay of AT/Dox/SFN against different treatments was further conducted. As shown in Fig. 8C, treating the mice with a high dose of free Dox (5 mg/kg) only resulted in mild tumor growth inhibition. The anticancer efficacies using single-loaded DDSs (AT/SFN and AT/Dox) at the same drug dose increased the anticancer benefits, but are still far from perfection. In contrast, AT/Dox/SFN using a low dose of drugs (1 mg/kg Dox and 3.06 mg/kg SFN) exerted the preferable outcome with significantly retarded growth in tumor volume. As confirmed in Fig. 8D, the histologic sections stained by hematoxylin-eosin (HE) revealed that AT/Dox/SFN treatment resulted in prominent cancer cell remission in the tumor tissue with the lowest level of proliferation (Ki67 staining) and highest apoptosis (TUNEL assay) without significant cytotoxicity on the subjects (Figure S10 and S11). In contrast,

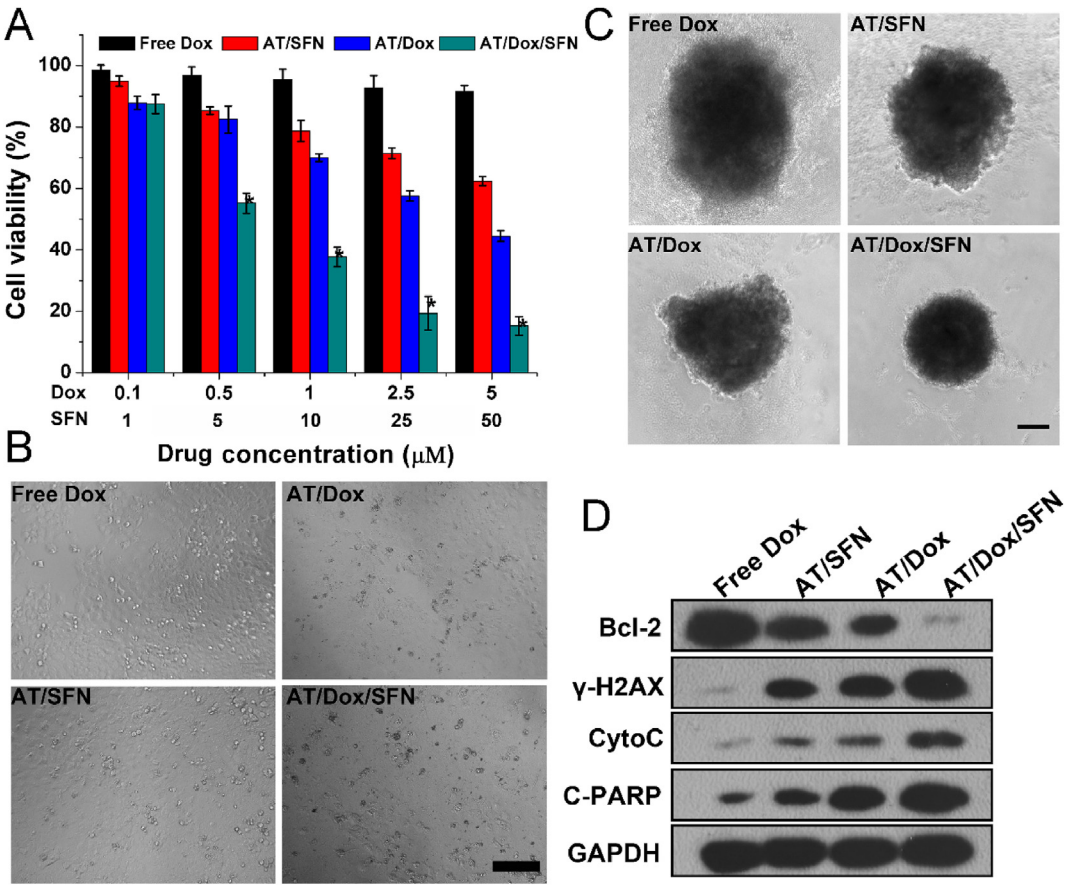

Fig. 7. *In vitro* anticancer effects of AT/Dox/SFN. (A) Cell viabilities of MCF-7/Adr cells incubated with free Dox, AT/Dox, AT/SFN or AT/Dox/SFN at different drug concentrations (0.1–5 μM for Dox, the mole ratio of SFN to Dox was fixed at 10) for 48 h $^*P < 0.05$ versus free Dox. (B) Representative optical images of MCF-7/Adr cells treated with different formulations (Dosage: 1 μM of Dox and 10 μM of SFN) for 48 h. Scale bar: 200 μm. (C)The optical image of MCTSs after different treatments with free Dox, AT/Dox, AT/SFN or AT/Dox/SFN for 4 Days (Dosage: 1 μM of Dox and 10 μM of SFN). Scale bar: 100 μm. (D) The protein levels within the MCTSs after being treated with different formulations at the end of the assay.

free Dox showed inefficient inhibition of tumor growth while induced significant toxicity to the subjects, including bodyweight loss (Figure S10) and multiple-organ pathology (Figure S11). As a result, it was suggested that AT/Dox/SFN could realize satisfactory anticancer performance at a low dosage of drugs, which was beneficial for safe cancer therapy in clinical practice.

3. Method

3.1. Materials

Sulforaphane (SFN) was obtained from Aladdin (Shanghai, China); Doxorubicin hydrochloride (Dox·HCl) was purchased from Dalian Meilun Biotech Co., Ltd. (Dalian, China); D-alpha Tocopheryl Polyethylene Glycol Succinate (TPGS) was offered by J&K Scientific (Beijing, China). All other solvents and reagents without specific statements were commercially available (of analytical grade) from Sigma-Aldrich (Missouri, USA).

3.2. Cell and animal models

MCF-7/Adr (human breast carcinoma cells with resistance to Dox) and NIH/3T3 (mouse embryonic fibroblast cells) cell lines were provided by the Institute of Biochemistry and Cell Biology (Shanghai, China) and cultured in Dulbecco's modified eagle medium (DMEM) supplied with 10% (v/v) fetal bovine serum (Gibco BRL, USA) in a humidified carbogen (95% air to 5% CO_2) at 37 °C (Thermo311, Thermo Fisher Scientific, USA).

Female New Zealand rabbits (200 g) and BALB/c nude mice (16 g) were provided by Shanghai Laboratory Animal Center (SLAC, China) and housed at 22 ± 2 °C with free access to diet. All animal experiments were approved by the Animal Care and Use Committee of Zhejiang University and strictly followed the guidelines for the care and use of laboratory animals.

The multi-cellular tumor spheroids (MCTSs) model was established using our previously reported protocol [47]. In brief, 96-well plates (Corning, USA) covered with autoclaved agarose were seeded with mixed MCF-7/Adr and NIH3T3 cells (1:1) at the density of 2×10^3 cells/well. The plates were returned to the incubator, and the formation of MCTSs was monitored using inverted optical/fluorescence microscope (TE2000-S, Nikon, Japan).

Cell suspensions at the density of 2×10^8 cells/mL (PBS, 0.01 M, pH 7.4) were subcutaneously inoculated to the flank of nude mice at the volume of 100 μL/per mouse and then allowed to grow into solid tumors for the establishment of MCF-7/Adr tumor xenograft model.

3.3. Preparation of AT/Dox/SFN

M-1 (0.085 g, 0.16 mmol), **M-2** (0.078 g, 0.16 mmol) and $Pd(PPh_3)_4$ (0.020 g, 5% e. q.) were dissolved in 10 mL toluene, 5 mL ethanol and 5 mL water with K_2CO_3 (0.60 g). The mixture was refluxed for 12 h under Ar atmosphere, and the organic phase was collected and dried with Na_2SO_4. Then the solvent was removed, and **M-3** (0.190 g), $Pd(PPh_3)_4$ (0.020 g, 5% e. q.) and $NaHCO_3$ (0.40 g) were added. The mixture was

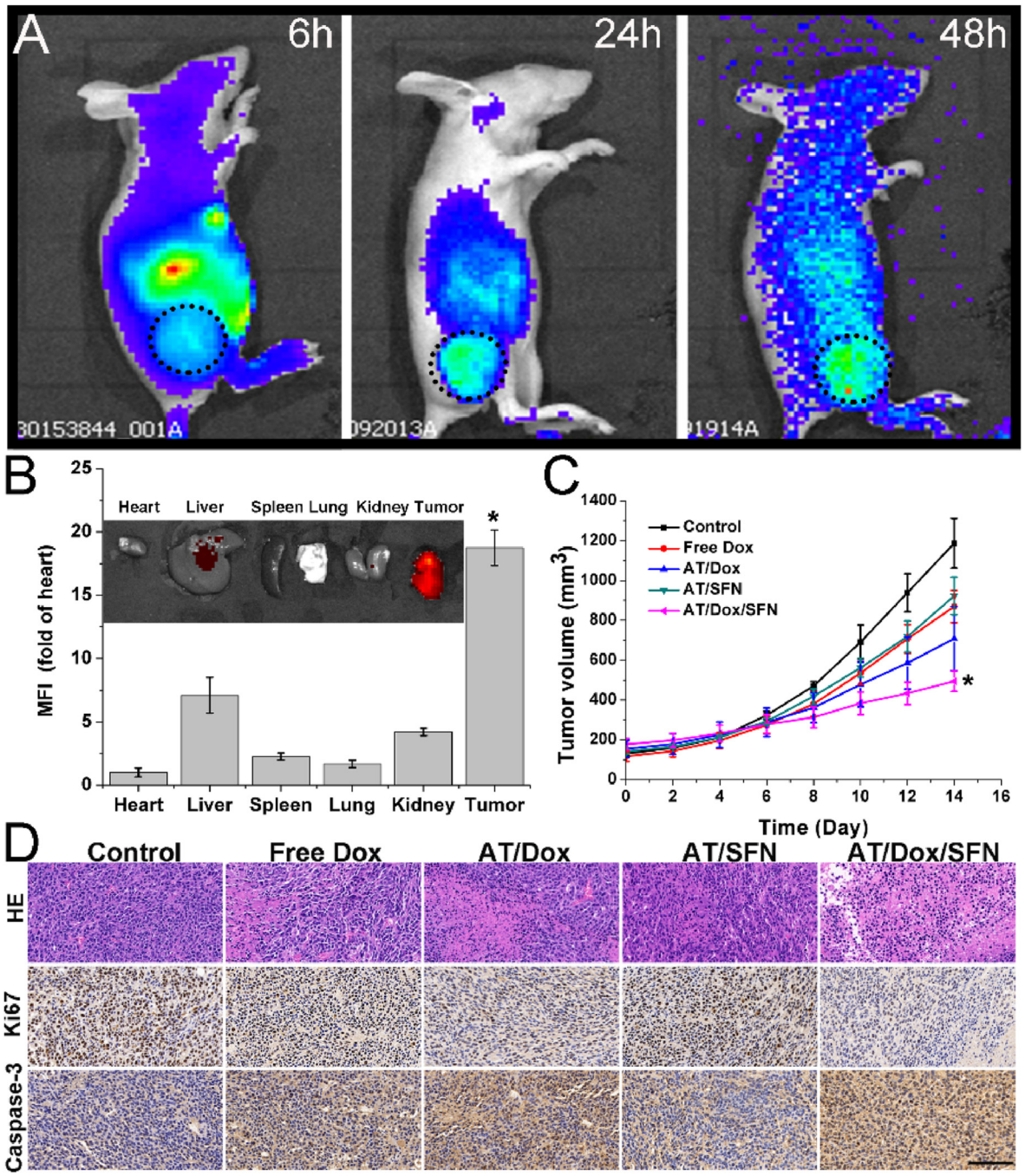

Fig. 8. *In vivo* tumor homing and anticancer efficacy of AT/Dox/SFN. (A) Time-dependent *in vivo* distribution of DiR-labeled AT/Dox/SFN in MCF-7/Adr oxgraft tumor model. (B) Representative *ex vivo* DiR fluorescence images and semi-quantitative analysis of dissected main organs and tumors (calculated as photon flux per mm^2 of tissues) at 48 h post-injection. *$P < 0.05$ versus Liver. (C) The tumor volume changes of model animal treated with saline, free Dox, AT/Dox, AT/SFN and AT/Dox/SFN (Dosage: 5 mg DOX/SFN per kg for free Dox, AT/Dox and AT/SFN; 1 mg/kg Dox and 3.06 mg/kg SFN for AT/Dox/SFN). *$P < 0.05$ versus Control. The measurement of tumor volumes was repeated every 2 days for two weeks. (D) Representative images (400 ×) of *ex vivo* tumor sections subjected to HE staining and immunohistology using TUNEL and Ki67 antibodies.

further dissolved in 30 mL THF and 15 mL water and then refluxed for 12 h under Ar atmosphere. **M-4** (0.008 g, 0.05 mmol) was added and reacted for another 12 h. Then **M-3** (0.190 g) was added again and reacted for 12 h. Afterward, the organic phase was collected and diluted with 50 mL CH_2Cl_2 and then washed with 50 mL water for three times. The resultant solution was dried by Na_2SO_4, and the solvent was removed. The resultant mixture was solved by THF and dropped into 300 mL hexane. The product was filtered and dried to give conjugated polymer as yellow solid (0.244 g). The H nuclear magnetic resonance (^{1}H NMR) spectra (400 MHz, $CDCl_3$) were: δ 7.68 (m, 3H), 7.57–7.39 (m, 9H), 7.21–7.11 (m, 12H), 4.31 (s, 2H), 3.66 (s, 155H), 2.27–1.97 (m, 5H), 1.95–1.77 (m, 3H), 1.65–0.97 (m, 17H), 0.95–0.70 (m, 5H). GPC data: $M_w = 6800$, $M_n = 4610$, PDI = 1.47.

The Dox·HCl was prepared into its base (Dox) and then loaded into AT with SFN by the co-precipitation method to give AT/Dox/SFN. In brief, Dox, SFN, AIE polymer and TPGS were dissolved in water-soluble organic solvent and sonicated to obtain a transparent solution. The organic phase was quickly injected into water (Millipore, USA) under sonication and then subjected to rotary evaporation to obtain the designated volume. The solution was centrifuged (8000 rpm for 10 min) and then stored at 4

°C until further usage. The single-loaded nanoparticles were prepared according to the same protocol using corresponding substances.

To determine the drug loading content of the nanoparticles, the lyophilized samples were weighted and dissolved in proper THF. After being diluted by ten times of acetonitrile, the mixture was sonicated and then filtered through a 0.22 μm filter (Millipore, USA) membrane. The Dox and SFN contents in the filtrate were measured at wavelengths of 480 nm and 270 nm, respectively, using physically mixed materials (subjected to the same treatments) as controls.

3.4. Characterizations

The ^{1}H NMR spectra were recorded at 400 MHz using Avance 400 spectrometer (Bruker, Germany), and the results were shown as parts per million (ppm) from the control (tetramethyl silicone). The ultraviolet–visible (UV–vis) absorption and fluorescence spectra were recorded by UV–vis spectrophotometer (UV-3600, Shimadzu, Japan) and fluorescence spectrometer (FLS-980, Edinburgh Instruments, UK), respectively. The molecular weight was assessed by gel permeation chromatography (GPC), and determined using the following protocol: Waters 244 (Waters, USA) machine and the column was PLgel MIXED-C (particle size: 5 μm; dimensions: 7.5 mm × 300 mm), the mobile phase/solvent was THF (flow rate of 0.6 mL/min) with polystyrene as a standard substance. The morphology and particle size were observed by transmission electron microscopy (TEM, 7650, Hitachi, Japan) and scanning electron microscopy (SEM, Regulus 8230, Hitachi, Japan). The size distribution and zeta potential were assessed using Zeta/Particle Analyzer (Litesizer 500, Anton Paar, Austria).

The colloidal stability and drug release of AT/Dox/SFN were assessed according to our previous report [47]. For stability assay, nanoparticles were diluted with PBS (pH 7.4) or 10% mouse plasma (1:10, v/v). Afterward, the changes in nanoparticle size were recorded every day for 7 days. For drug release, AT/Dox/SFN was placed into dialysis bags (MWCO: 7 KDa) and immersed in plastic tubes containing phosphate buffer (pH 7.4) with 0.5% Tween 80. The plastic tubes were fixed in a thermostatic shaker at 37°C with gentle shaking (100 rpm). At predetermined time intervals, 200 μL of the buffer was withdrawn for analysis. The Dox concentration was determined using fluorescence spectrophotometer (Em = 590 nm, Ex = 485 nm) and SFN concentration was determined using high performance liquid chromatography (HPLC, column: diamonsil C18; detection wavelength: 229 nm; mobile phase: methanol/water (1:9, v/v) containing 0.1% formic acid with pH of 4.0; flow rate: 1 mL/min; temperature: 30 °C).

The hemolysis of AT/Dox/SFN against was red blood cells (RBCs) assessed according to our previous report [47]. In brief, 2% suspension of RBCs (New Zealand rabbit) was incubated with a series concentration of AT/Dox/SFN for 1 h at 37 °C. Afterward, the supernatant was collected by centrifugation (3000 rpm × 10 min), and its absorbance at 545 nm was measured by UV–vis spectrophotometer.

3.5. AIE imaging and FERT-indicated drug release

MCF-7/Adr cells were seeded on 35 mm diameter glass dishes (Corning, USA; cell density: 2 × 10^4/dish) and allowed to grow into 60–70% confluence. Afterward, the primary culture medium was discarded and supplied with fresh serum-free DMEM containing free Dox, AT or AT/Dox/SFN (Dox concentration: 1 μM, the mole ratio of SFN to Dox was fixed at 10). After incubation for designated time intervals, the culture medium was removed, and the dishes were rinsed three times with PBS and then fixed with 4% formaldehyde (15 min). The images were captured using a confocal laser scanning microscope (CLSM, BX61W1-FV3000, Olympus, Japan). The fluorescence of AT was recorded at Ex = 405 nm/Em = 422–522 nm (Donor channel). The Dox was observed at Ex = 559 nm/Em = 575–675 nm (Acceptor channel). The fluorescence from FRET was observed at Ex = 405 nm/Em = 575–675 nm (FRET channel).

3.6. Modulation of intracellular redox homeostasis

MCF-7/Adr cells were seeded in 24-well plates (Corning) at the cell density of 5 × 10^4 cells/well and allowed to grow overnight to afford 50–60% confluence. Afterward, cells were incubated with SFN, TPGS or AT/SFN (Concentrations: 10 μM of SFN and/or 5 μg/mL of TPGS) for different time intervals (6 or 12 h). At the end of incubation, cells were firstly incubated with DCFH-DA (10 μM for 30 min) and then subjected to CLSM observation.

MCF-7/Adr cells were seeded in 6 well plates (Corning; 1 × 10^5 cells/well) overnight for 50–60% confluence. Afterward, cells were incubated with SFN, TPGS or AT/SFN for another 12 h. Cells from each group were recruited in equal numbers, and the intracellular GSH level was detected using the corresponding kit (Solarbio Life Science, Beijing, China) according to the manufacturer's instructions.

MCF-7/Adr cells seeded in 150-mm culture dishes (Corning) were allowed to grow into 80% confluence and then incubated with SFN, TPGS or AT/SFN for different time intervals (4, 8 and 12 h). Afterward, the mitochondria of cells were isolated by Mitochondrial Extraction Kit (Solarbio) on ice, and the mitochondrial swelling degree (OD_{530nm}) was compared against the control group (the mitochondria from untreated cells subjected to the same procedure) according to our previous report [48]. Additional, the mitochondrial membrane potential of cells at 8 h post incubation was stained using JC-1 according to the manufacturer's instructions (Beyotime, Shanghai, China) and then visualized by CLSM to reflect the damage of mitochondria.

Cells in 6-well plates were treated with SFN, TPGS or AT/SFN for different time intervals as mentioned above. Afterward, cells were lysed, followed by centrifugation for 5 min at 12,000 g. The resulting supernatant was collected to measure the intracellular ATP content according to the instruction of ATP Content Assay Kit (Solarbio).

3.7. MDR reversion and positive feedback for uptake

MCF-7/Adr cells were seeded into 24-well plates and incubated with SFN, TPGS or AT/SFN for 12 h. Afterward, free Dox was added into the solution to achieve a final drug concentration of 5 μM and further incubated with the cells for another 4 h. Finally, the intracellular Dox signal was imaged using CLSM.

MCF-7/Adr cells were incubated with AT/SFN for different time intervals (4, 8 and 12 h). Afterward, the primary culture medium was removed and replaced with the fresh medium containing AT/Dox/SFN (Dox concentration: 2 μM) for 4 h. Finally, the intracellular Dox content was determined using our previously reported protocol [24]. In brief, cells were immersed in Dox extracting solution (ethanol: 0.6 M HCl, 1:1, v/v) and pulverized by ultrasonication (400 W, 40 times) in ice. The mixture was stood for 24 h and then centrifuged (12000 rpm, 10min) to collect the supernatant, and the Dox within was determined as mentioned above.

The MCF-7/Adr tumor-bearing nude mice were intratumorally administrated with 50 μL of AT/SFN (SFN concentration: 100 μM). At different time intervals (24 and 48 h) post-injection, tumor tissues were collected and subjected to immunohistochemical (IHC) staining of P-gp protein. Additionally, the tumor tissues were treated with Collagenase (Sigma-Aldrich, USA) according to the manufacturer's instructions. The obtained free cancer cells were seeded on the 35 mm diameter glass dishes (Corning; cell density: 3 × 10^5/dish) and cultured with AT/Dox/SFN for 4 h. Finally, the cells were treated with 2% bovine serum albumin (BSA), stained with anti-P-gp monoclonal antibody and secondary antibody according to our previous report [49], followed by CLSM observations. AT/SFN untreated tumor tissues subjected to the same procedures were taken as controls.

3.8. Neighboring effect and drug penetration

In brief, MCF-7/Adr cells seeded on 24-well plates with coverslips

were pretreated with the AT/Dox/SFN at a Dox concentration of 10 μM for different time intervals (12 and 24 h). The pretreated cells (A) were washed with PBS and then co-incubated with the fresh cells on a coverslip (B) for 24 h in the fresh culture medium. The cells (coverslip B) were then washed by ice-cold PBS thrice, stained with Annexin V-FITC (Solarbio) according to the manufacturer's protocol and observed using CLSM.

The MCTSs were incubated with fresh serum-free DMEM containing free Dox or AT/Dox/SFN at the Dox concentration of 5 μM for 24 h. Then, the MCTSs were fixed with 4% formaldehyde (15 min) and then observed using tomoscan of Z-stack imaging by CLSM.

When the tumor volume of the MCF-7/Adr xenograft tumor model reached 200 mm^3, the mice were intratumorally administrated with 50 μL of free Dox or AT/Dox/SFN (Dox concentration: 10 μM, the mole ratio of SFN to Dox was fixed at 10). At 48 h post-injection, tumor tissues were collected and washed by PBS, followed by frozen cryotomy. The tumor tissues were subjected to FITC-CD31 antibody (Solarbio) staining, and the distribution of Dox signal within the whole tumor tissue was observed using the full scan function of CLSM.

3.9. In vitro cytotoxicity assay

The cytotoxicity of AIE polymer, free Dox or drug-loaded nanoparticles against MCF-7/Adr cells was determined by MTT assays [50]. In brief, MCF-7/Adr seeded in 96-well plates (2×10^3 cells/well) overnight were incubated with AIE polymer, free Dox, AT/Dox, AT/SFN or AT/Dox/SFN at various drugs (The molar ratio of SFN to Dox was fixed at 10) or nanoparticle concentrations for 48 h. Afterward, MTT (20 μL, 5 mg/mL) was added for another 4 h of incubation at 37 °C. Finally, the formazan crystals were dissolved in 200 μL of DMSO, and the absorbance at 570 nm was determined using a microplate reader (Model 680, Bio-Rad, USA). Moreover, the cell morphology and viability were also visualized by an optical microscope.

MCTSs were incubated with free Dox, AT/Dox, AT/SFN or AT/Dox/SFN at the Dox concentration of 1 μM (The mole ratio of SFN to Dox was fixed at 10) at 37 °C for 4 days. The diameter of the spheroids was recorded using an optical microscope. At the end of the test, the protein levels (Bcl-2, γ-H2AX, cytochrome C, PAPR) in cells were determined using western blot assay according to previous reports and our experiments [7,51].

3.10. In vivo tumor targeting assay

For *in vivo* imaging analysis, near-infrared (NIR) probe DiR was loaded into the nanoparticles during the drug loading procedure. Subsequently, DiR-loaded AT/Dox/SFN was intravenously injected into the tumor-bearing nude mice at a dose of 20 μg DiR/kg. At different time intervals (6, 24 and 48 h) post-injection, the distribution of nanoparticles was studied using an *in vivo* imaging system (Maestro In-vivo Imaging System, USA). At the end of living imaging, the main organs (heart, liver, spleen, lung, kidney) and tumor tissues were excised from the mice for *ex vivo* imaging using the same system.

3.11. In vivo antitumor evaluation

The MCF-7/Adr tumor-bearing nude mice were divided into different groups randomly, and this day was set as day 0. Mice were administered intravenously with saline, free Dox, AT/Dox, AT/SFN or AT/Dox/SFN (Dosage: 5 mg DOX/SFN per kg for free Dox, AT/Dox and AT/SFN; 1 mg/kg Dox and 5 mg/kg SFN for AT/Dox/SFN) every 2 days for 7 times. Tumor volume and body weight were recorded every 2 days before drug administration.

At the end of the test, one mouse was randomly selected and sacrificed. The main organs (heart, liver, spleen, lung, kidney) and tumor tissue were fixed, embedded in paraffin and then subjected to hematoxylin and eosin (H&E) staining, Ki67 and TUNEL assays.

4. Conclusion

In summary, we reported on the fabrication and characterization of an ultrasmall AIE polymer-based nanoparticle co-delivering Dox and SFN (AT/Dox/SFN) to combat MDR cancer. Our results demonstrated that the AT/Dox/SFN as a theranostic platform can self-report its location using AIE fluorescence and drug release profile through FRET signal. Most importantly, the introduced TPGS and SFN in the DDS can effectively modulate the redox homeostasis of MCF-7/Adr cells, which triggers following mitochondria damage and ATP deficiency to realize the reverse of MDR phenotype. This phenomenon further offers enhanced intracellular drug accumulation as well as nanoparticle uptake, which is beneficial to augmenting the "neighboring effect" of the DDS in the tumor. Cooperated with its size advantage, the AT/Dox/SFN is demonstrated to potentiate the drug delivery into the deep tumor tissue. As a result, the AT/Dox/SFN can effectively suppress the proliferation of MCF-7/Adr cells *in vitro*, and especially, effectively inhibits the growth of MCF-7/Adr tumor *in vivo* at a low dosage of drugs. This work provides an ultrasmall AIE polymer-based nanoplatform with self-indication capacity for the delivery of various drugs, which offers a good template for the future development of more advanced theranostic DDSs.

Credit author statement

Shaoqing Chen: Methodology, Formal analysis, Investigation, Validation, Resources; **Ziyu Wang**: Methodology, Formal analysis, Investigation, Validation, Data Curation, Visualization; **Li Liu**: Formal analysis, Investigation; **Yuting Li**: Formal analysis, Investigation; **Xinye Ni**: Conceptualization, Resources, Supervision, Project administration, Writing - Review & Editing; **Hong Yuan**: Conceptualization, Resources, Supervision, Project administration, Writing - Review & Editing; **Cheng Wang**: Conceptualization, Data Curation, Writing - Original Draft, Visualization, Funding acquisition.

Declaration of competing interest

The authors declare that they have no known competing financial interests or personal relationships that could have appeared to influence the work reported in this paper.

Acknowledgments

This work was supported by China Postdoctoral Science Foundation Funded Project (No. 2021M690482) and Jiangsu Postdoctoral Science Foundation Funded Project (No. 2021K014A). We acknowledge the tissue slide preparation, staining, and imaging services provided by Record Biological Technology Co., Ltd. (Shanghai, China).

Appendix A. Supplementary data

Supplementary data to this article can be found online at https://doi.org/10.1016/j.mtbio.2022.100396.

References

[1] H. Wu, D. Zhong, Z. Zhang, Y. Li, X. Zhang, Y. Li, Z. Zhang, X. Xu, J. Yang, Z. Gu, Bioinspired artificial tobacco mosaic virus with combined oncolytic properties to completely destroy multidrug-resistant cancer, Adv. Mater. 32 (9) (2020), 1904958.
[2] W. Ma, Q. Chen, W. Xu, M. Yu, Y. Yang, B. Zou, Y.S. Zhang, J. Ding, Z. Yu, Self-targeting visualizable hyaluronate nanogel for synchronized intracellular release of doxorubicin and cisplatin in combating multidrug-resistant breast cancer, Nano Res. 14 (3) (2021) 846–857.
[3] Y. Xiong, C. Xiao, Z. Li, X. Yang, Engineering nanomedicine for glutathione depletion-augmented cancer therapy, Chem. Soc. Rev. 50 (10) (2021) 6013–6041.
[4] X. Xiao, K. Wang, Q. Zong, Y. Tu, Y. Dong, Y. Yuan, Polyprodrug with glutathione depletion and cascade drug activation for multi-drug resistance reversal, Biomaterials 270 (2021), 120649.

[5] N. Gong, X. Ma, X. Ye, Q. Zhou, X. Chen, X. Tan, S. Yao, S. Huo, T. Zhang, S. Chen, Carbon-dot-supported atomically dispersed gold as a mitochondrial oxidative stress amplifier for cancer treatment, Nat. Nanotechnol. 14 (4) (2019) 379–387.

[6] S.P. Kubli, C. Bassi, C. Roux, A. Wakeham, C. Göbl, W. Zhou, S.M. Jafari, B. Snow, L. Jones, L. Palomero, AhR controls redox homeostasis and shapes the tumor microenvironment in BRCA1-associated breast cancer, Proc. Natl. Acad. Sci. USA 116 (9) (2019) 3604–3613.

[7] Y. Xu, X. Han, Y. Li, H. Min, X. Zhao, Y. Zhang, Y. Qi, J. Shi, S. Qi, Y. Bao, Sulforaphane mediates glutathione depletion via polymeric nanoparticles to restore cisplatin chemosensitivity, ACS Nano 13 (11) (2019) 13445–13455.

[8] Z. Zhu, S. Du, Y. Du, J. Ren, G. Ying, Z. Yan, Glutathione reductase mediates drug resistance in glioblastoma cells by regulating redox homeostasis, J. Neurochem. 144 (1) (2018) 93–104.

[9] S.C. Nunes, J. Serpa, Glutathione in ovarian cancer: a double-edged sword, Int. J. Mol. Sci. 19 (7) (2018) 1882.

[10] M. He, L. Yu, Y. Yang, B. Zou, W. Ma, M. Yu, J. Lu, G. Xiong, Z. Yu, A. Li, Delivery of triptolide with reduction-sensitive polymer nanoparticles for liver cancer therapy on patient-derived xenografts models, Chin. Chem. Lett. 31 (12) (2020) 3178–3182.

[11] J. Yan, Q. Wu, Z. Zhao, J. Wu, H. Ye, Q. Liang, Z. Zhou, M. Hou, X. Li, Y. Liu, L. Yin, Light-assisted hierarchical intratumoral penetration and programmed antitumor therapy based on tumor microenvironment (TME)-amendatory and self-adaptive polymeric nanoclusters, Biomaterials 255 (2020), 120166.

[12] K. Soni, M. Rizwanullah, K. Kohli, Development and optimization of sulforaphane-loaded nanostructured lipid carriers by the Box-Behnken design for improved oral efficacy against cancer: in vitro, ex vivo and in vivo assessments, Artif. Cell Nanomed. Biotechnol. 46 (sup1) (2018) 15–31.

[13] M.M. Kamal, S. Nazzal, Novel sulforaphane-enabled self-microemulsifying delivery systems (SFN-SMEDDS) of taxanes: formulation development and in vitro cytotoxicity against breast cancer cells, Int. J. Pharm. 536 (1) (2018) 187–198.

[14] W. Lu, F. Du, X. Zhao, L. Shi, S. Shuang, X.T. Cui, C. Dong, Sulforaphane-conjugated carbon dots: a versatile nanosystem for targeted imaging and inhibition of EGFR-overexpressing cancer cells, ACS Biomater. Sci. Eng. 5 (9) (2019) 4692–4699.

[15] P.J. Thornalley, Isothiocyanates: mechanism of cancer chemopreventive action, Anti Cancer Drugs 13 (4) (2002) 331–338.

[16] C. Pais-Silva, D. de Melo-Diogo, I.J. Correia, IR780-loaded TPGS-TOS micelles for breast cancer photodynamic therapy, Eur. J. Pharm. Biopharm. 113 (2017) 108–117.

[17] Z. Su, M. Chen, Y. Xiao, M. Sun, L. Zong, S. Asghar, M. Dong, H. Li, Q. Ping, C. Zhang, ROS-triggered and regenerating anticancer nanosystem: an effective strategy to subdue tumor's multidrug resistance, J. Contr. Release 196 (2014) 370–383.

[18] C. Yang, T. Wu, Y. Qi, Z. Zhang, Recent advances in the application of vitamin E TPGS for drug delivery, Theranostics 8 (2) (2018) 464.

[19] K. Kessenbrock, V. Plaks, Z. Werb, Matrix metalloproteinases: regulators of the tumor microenvironment, Cell 141 (1) (2010) 52–67.

[20] T.L. Whiteside, The tumor microenvironment and its role in promoting tumor growth, Oncogene 27 (45) (2008) 5904–5912.

[21] C. Wong, T. Stylianopoulos, J. Cui, J. Martin, V.P. Chauhan, W. Jiang, Z. Popović, R.K. Jain, M.G. Bawendi, D. Fukumura, Multistage nanoparticle delivery system for deep penetration into tumor tissue, Proc. Natl. Acad. Sci. USA 108 (6) (2011) 2426–2431.

[22] D. Ni, H. Ding, S. Liu, H. Yue, Y. Bao, Z. Wang, Z. Su, W. Wei, G. Ma, Superior intratumoral penetration of paclitaxel nanodots strengthens tumor restriction and metastasis prevention, Small 11 (21) (2015) 2518–2526.

[23] D. Dehaini, R.H. Fang, B.T. Luk, Z. Pang, C.-M.J. Hu, A.V. Kroll, C.L. Yu, W. Gao, L. Zhang, Ultra-small lipid–polymer hybrid nanoparticles for tumor-penetrating drug delivery, Nanoscale 8 (30) (2016) 14411–14419.

[24] C. Wang, S. Chen, Y. Wang, X. Liu, F. Hu, J. Sun, H. Yuan, Lipase-triggered water-responsive “Pandora's Box” for cancer therapy: toward induced neighboring effect and enhanced drug penetration, Adv. Mater. 30 (14) (2018), 1706407.

[25] S. Guo, Y. Wang, L. Miao, Z. Xu, C.M. Lin, Y. Zhang, L. Huang, Lipid-coated cisplatin nanoparticles induce neighboring effect and exhibit enhanced anticancer efficacy, ACS Nano 7 (11) (2013) 9896–9904.

[26] Y. Pei, Z. Wang, C. Wang, Recent progress in polymeric AIE-active drug delivery systems: design and application, Mol. Pharm. 18 (11) (2021) 3951–3965.

[27] Z. Wang, C. Wang, Q. Gan, Y. Cao, H. Yuan, D. Hua, Donor–acceptor-type conjugated polymer-based multicolored drug carriers with tunable aggregation-induced emission behavior for self-illuminating cancer therapy, ACS Appl. Mater. Interfaces 11 (45) (2019) 41853–41861.

[28] X. Qiu, Y. Qu, B. Guo, H. Zheng, F. Meng, Z. Zhong, Micellar paclitaxel boosts ICD and chemo-immunotherapy of metastatic triple negative breast cancer, J. Contr. Release 341 (2022) 498–510.

[29] G. Chen, Y. Yang, Q. Xu, M. Ling, H. Lin, W. Ma, R. Sun, Y. Xu, X. Liu, N. Li, Self-amplification of tumor oxidative stress with degradable metallic complexes for synergistic cascade tumor therapy, Nano Lett. 20 (11) (2020) 8141–8150.

[30] L. Yu, Z. Wang, Z. Mo, B. Zou, Y. Yang, R. Sun, W. Ma, M. Yu, S. Zhang, Z. Yu, Synergetic delivery of triptolide and Ce6 with light-activatable liposomes for efficient hepatocellular carcinoma therapy, Acta Pharm. Sin. B 11 (7) (2021) 2004–2015.

[31] Z. Cao, N.N.M. Adnan, G. Wang, A. Rawal, B. Shi, R. Liu, K. Liang, L. Zhao, J.J. Gooding, C. Boyer, Enhanced colloidal stability and protein resistance of layered double hydroxide nanoparticles with phosphonic acid-terminated PEG coating for drug delivery, J. Colloid Interface Sci. 521 (2018) 242–251.

[32] J. Zhao, P. Xie, C. Ye, C. Wu, W. Han, M. Huang, S. Wang, H. Chen, Outside-in synthesis of mesoporous silica/molybdenum disulfide nanoparticles for antitumor application, Chem. Eng. J. 351 (2018) 157–168.

[33] H. Zhu, H. Chen, X. Zeng, Z. Wang, X. Zhang, Y. Wu, Y. Gao, J. Zhang, K. Liu, R. Liu, Co-delivery of chemotherapeutic drugs with vitamin E TPGS by porous PLGA nanoparticles for enhanced chemotherapy against multi-drug resistance, Biomaterials 35 (7) (2014) 2391–2400.

[34] D. Pooja, H. Kulhari, M.K. Singh, S. Mukherjee, S.S. Rachamalla, R. Sistla, Dendrimer–TPGS mixed micelles for enhanced solubility and cellular toxicity of taxanes, Colloids Surf. B Biointerfaces 121 (2014) 461–468.

[35] X. Gu, Y. Wei, Q. Fan, H. Sun, R. Cheng, Z. Zhong, C. Deng, cRGD-decorated biodegradable polytyrosine nanoparticles for robust encapsulation and targeted delivery of doxorubicin to colorectal cancer in vivo, J. Contr. Release 301 (2019) 110–118.

[36] W. Zhuang, B. Ma, J. Hu, J. Jiang, G. Li, L. Yang, Y. Wang, Two-photon AIE luminogen labeled multifunctional polymeric micelles for theranostics, Theranostics 9 (22) (2019) 6618.

[37] X. Kong, B. Dong, X. Song, C. Wang, N. Zhang, W. Lin, Dual turn-on fluorescence signal-based controlled release system for real-time monitoring of drug release dynamics in living cells and tumor tissues, Theranostics 8 (3) (2018) 800.

[38] W.H. Chen, W.C. Liao, Y.S. Sohn, M. Fadeev, A. Cecconello, R. Nechushtai, I. Willner, Stimuli-Responsive nucleic acid-based polyacrylamide hydrogel-coated metal–organic framework nanoparticles for controlled drug release, Adv. Funct. Mater. 28 (8) (2018), 1705137.

[39] T.C. Jorgenson, W. Zhong, T.D. Oberley, Redox imbalance and biochemical changes in cancer, Cancer Res. 73 (20) (2013) 6118–6123.

[40] I.S. Mohammad, W. He, L. Yin, Understanding of human ATP binding cassette superfamily and novel multidrug resistance modulators to overcome MDR, Biomed. Pharmacother. 100 (2018) 335–348.

[41] H. Wang, Z. Feng, Y. Qin, J. Wang, B. Xu, Nucleopeptide assemblies selectively sequester ATP in cancer cells to increase the efficacy of doxorubicin, Angew. Chem. 130 (18) (2018) 5025–5029.

[42] Y. Sun, C. Wang, Q. Meng, Z. Liu, X. Huo, P. Sun, H. Sun, X. Ma, J. Peng, K. Liu, Targeting P-glycoprotein and SORCIN: dihydromyricetin strengthens anti-proliferative efficiency of adriamycin via MAPK/ERK and Ca2+-mediated apoptosis pathways in MCF-7/ADR and K562/ADR, J. Cell. Physiol. 233 (4) (2018) 3066–3079.

[43] C. Ju, R. Mo, J. Xue, L. Zhang, Z. Zhao, L. Xue, Q. Ping, C. Zhang, Sequential intra-intercellular nanoparticle delivery system for deep tumor penetration, Angew. Chem. Int. Ed. 53 (24) (2014) 6253–6258.

[44] Y. Zhu, Y. Guo, M. Liu, L. Wei, X. Wang, An oroxylin A-loaded aggregation-induced emission active polymeric system greatly increased the antitumor efficacy against squamous cell carcinoma, J. Mater. Chem. B 8 (10) (2020) 2040–2047.

[45] Q. Huang, J. Cheng, Y. Tang, Y. Wu, D. Xia, Y. Zheng, M. Guo, Significantly red-shifted emissions of nonconventional AIE polymers containing zwitterionic components, Macromol. Rapid Commun. 42 (14) (2021), 2100174.

[46] D. Zhao, W. Tao, S. Li, Y. Chen, Y. Sun, Z. He, B. Sun, J. Sun, Apoptotic body–mediated intercellular delivery for enhanced drug penetration and whole tumor destruction, Sci. Adv. 7 (16) (2021), eabg0880.

[47] C. Wang, M. Han, X. Liu, S. Chen, F. Hu, J. Sun, H. Yuan, Mitoxantrone-preloaded water-responsive phospholipid-amorphous calcium carbonate hybrid nanoparticles for targeted and effective cancer therapy, Int. J. Nanomed. 14 (2019) 1503–1517, https://doi.org/10.2147/ijn.S193976.

[48] C. Wang, F. Yu, X. Liu, S. Chen, R. Wu, R. Zhao, F. Hu, H. Yuan, Cancer-specific therapy by artificial modulation of intracellular calcium concentration, Adv. Healthcare Mater. 8 (18) (2019), 1900501.

[49] S.-Q. Chen, C. Wang, S. Tao, Y.-X. Wang, F.-Q. Hu, H. Yuan, Rational design of redox-responsive and P-gp-Inhibitory lipid nanoparticles with high entrapment of paclitaxel for tumor therapy, Adv. Healthcare Mater. 7 (17) (2018), 1800485, https://doi.org/10.1002/adhm.201800485.

[50] C. Wang, S. Chen, F. Yu, J. Lv, R. Zhao, F. Hu, H. Yuan, Dual-channel theranostic system for quantitative self-indication and low-temperature synergistic therapy of cancer, Small 17 (10) (2021), 2007953.

[51] C. Wang, Z. Wang, S. Chen, P. Cui, L. Qiu, S. Zhou, H. Jiang, P. Jiang, J. Wang, Modulation of aggregation-caused quenching to aggregation-induced emission: finding a biocompatible polymeric theranostics platform for cancer therapy, Macromol. Rapid Commun. 42 (19) (2021), 2100264.